Results in Physics 15 (2019) 102577

Contents lists available at ScienceDirect

Results in Physics

journal homepage: www.elsevier.com/locate/rinp

Investigation of terahertz radiations in both time and frequency domains via the Cherenkov model

Yamin Chen, Jiayu Zhao*

Shanghai Key Laboratory of Modern Optical System, School of Optical-Electrical and Computer Engineering, University of Shanghai for Science and Technology, Shanghai 200093, China

ARTICLE INFO

Keywords:
Terahertz
Filamentation
Longitudinal wave
Cherenkov

ABSTRACT

In this work, deduced from the well-known Cherenkov model [Phys. Rev. Lett. 2007, 98, 235002], calculation methods of temporal and spectral waveforms of the electromagnetic (EM) radiation driven by the longitudinal current during single-colour filamentation have been resolved. It was discovered that, the plasma density and the electron collision frequency of the filament, as well as the pulse duration of the pumping laser, play crucial roles on the generated peak frequency and width of the EM spectrum. Afterwards, calculations of the EM emission have been concentrated on terahertz (THz) band, whose generation, detection and enhancement were investigated, respectively, with the developed calculation method. The corresponding theoretical results have been well supported by experimental observations of ourselves or in the literature.

Introduction

In recent years, longitudinally polarized waves have attracted intense attention in the community for its many promising applications, such as particle acceleration [1], fluorescent imaging [2], laser machining [3], optical tweezers [4] and microscopy [5], etc. Specifically in terahertz (THz) spectral region, such a longitudinal field acquires additional abilities, e.g. observing various low-energy elementary excitations, or even controlling them via THz-dipole interactions [6]. Thus, THz sources with longitudinal wave output have been developed, including velocity-mismatched optical rectification [7], segmented GaP crystals [8] and photoconductive antennas with radial electrode geometries [9–12].

Another practical way of creating a strong longitudinal THz electric field (~1 kV/cm [6]) is by means of focusing a conically propagating THz beam with radial polarization, which is generated from an air plasma filament induced by a single-colour femtosecond laser pulse [6,13,14]. The underlying mechanism of this physical process is normally understood as a Cherenkov-type THz wave emission from a dipole-like structure oscillating longitudinally in the plasma column [13,14]. In this work, based on this Cherenkov electromagnetic (EM) emission model [15], theoretical and experimental studies on the EM temporal and spectral waveforms (mainly in THz band) radiated from the laser filament have been carried out.

Briefly, in Section "Calculation methods of EM waveforms in both time and frequency domains", the EM radiation induced by the longitudinal current during single-colour filamentation has been analytically solved in both time and frequency domains. It has been found that the calculated EM waveforms agreed well with the previous experimental reports [16], proving the validity of our calculation method. Then, in Section "Effects of three characteristic parameters on the generated EM spectrum", attention has been paid to three characteristic parameters, i.e., the free electron density (N_e) and the electron collision frequency (ν_e) of the plasma filament, as well as the pump laser pulse duration (τ_L), whose influences on the EM spectrum output have been discussed. It can be seen that the N_e value mainly determines the spectral peak frequency, and ν_e value indicates the spectral peak width, while τ_L affects both. Next, in the following three sections, comparisons have been performed between several calculated and experimental results, including the THz generation along the axis of the plasma filament [17], the THz detection by electro-optic (EO) sampling [18], and the THz enhancement with a longitudinal static electric field positioned along the filament [15]. The demonstrated consistencies have further verified our calculation method.

Theoretical and experimental results

The well-known Cherenkov radiation, firstly reported by P. A. Cherenkov in 1934 [19], describes notable properties of radiation which appears during the motion of fast, electrically charged particles

* Corresponding author.
E-mail address: zhaojiayu@usst.edu.cn (J. Zhao).

https://doi.org/10.1016/j.rinp.2019.102577
Received 22 April 2019; Received in revised form 4 August 2019; Accepted 6 August 2019
Available online 09 August 2019

through a substance. According to the subsequently established theory by I. M. Frank and I. E. Tamm [20], an electron moving in a medium of refractive index n with a velocity exceeding that of light in the same medium ($\beta > 1/n$) is liable to emit light which must be propagated in a direction forming an angle θ with the path of the electron. This angle is determined by the equation of $\cos\theta = 1/\beta n$, where β is the ratio of the electron velocity to that of light in vacuum.

In practice, the moving particle could be a dipole-like electric charge [13], which might decrease the emission efficiency, but does not suppress it completely. On the other hand, the speed of the particle doesn't have to be considerably larger than that of the light in the medium, as long as its moving trajectory has a finite length [13]. In this situation, the Cherenkov radiation holds also some features of the well-known transition radiation [21], for which reason the Cherenkov mechanism was also named "transition-Cherenkov emission" by the authors of Ref. [13]. However, it is worth noting that, this "transition-Cherenkov emission" cannot be understood as a real mixture of the two physical processes [22,23], since no "transition" of particles at boundaries between two media was actually involved in Ref. [13,15,24].

Calculation methods of EM waveforms in both time and frequency domains

During single-colour femtosecond laser filamentation in air, a longitudinal current is created, associated with the plasma wave excitation in the wake of the laser pulse [15,24]. For a laser pulse with duration of τ_L, maximum intensity of I_0, and a $\sin^2$ temporal shape of $I(t) = I_0\sin^2(\pi t/\tau_L)$, the wake current spectrum $j_z(\omega)$ is written as [15]:

$$j_z(\omega) = \varepsilon_0 E_L \omega_{pe} \frac{\omega + 2i\nu_e}{\omega_{pe}^2 - \omega^2 + i\nu_e\omega} \times \frac{\sin(\omega\tau_L/2)}{1-(\omega\tau_L/2\pi)^2} \exp\left(-\frac{i\omega\tau_L}{2}\right) \quad (1)$$

where $E_L = e\omega_{pe} I_0 / 2m_e \varepsilon_0 c^2\omega_0^2$ is the amplitude of the plasma wave driven by the laser ponderomotive force; $\omega_{pe} = (e^2 N_e / m_e \varepsilon_0)^{1/2}$ is the plasma frequency; N_e is the plasma density; ω_0 is the laser frequency, and ν_e is the electron collision frequency. Employing typical parameter values as follows: $\lambda = 800$ nm, $\tau_L = 50$ fs, $I_0 = 1\times10^{14}$ W/cm^2, $\nu_e = 2$ THz and $N_e = 1\times10^{17}$ cm^{-3}, an example of $j_z(\omega)$ was calculated and shown in Fig. 1(a) as the black line. One can see that the current spectrum has a sharp peak located at low frequency of several terahertz, followed by a series of step-down high-frequency components. The origin of these features will be discussed in detail in Section "Effects of three characteristic parameters on the generated EM spectrum".

On the other hand, it is well known that during free electron oscillation, EM emission occurs with amplitude proportional to the differentiation of the current in the time domain by $E(t)\propto\partial j(t)/\partial t$ [25]. If further applying Fourier transformation (FT) on both sides of the differential formula, one gets $E(\omega)\propto i\omega j(\omega)$. Thus, the EM spectrum radiation during single-colour filamentation is determined by

$$E_z(\omega) \propto i\omega\varepsilon_0 E_L \omega_{pe} \frac{\omega + 2i\nu_e}{\omega_{pe}^2 - \omega^2 + i\nu_e\omega} \times \frac{\sin(\omega\tau_L/2)}{1-(\omega\tau_L/2\pi)^2} \exp\left(-\frac{i\omega\tau_L}{2}\right) \quad (2)$$

and the calculation result is also displayed in Fig. 1(a) as the red dashed line. It can be seen that its step-down high-frequency components relatively increased compared with the low-frequency sharp spectral peak.

In next step, inverse Fourier transformations (iFTs) were performed on both of the current spectrum $j_z(\omega)$ and EM spectrum $E_z(\omega)$, in order to obtain their corresponding signals in time domain. The resulted temporal profiles of $j_z(t)$ and $E_z(t)$ are displayed in Fig. 1(b) as the black line and the red dashed line, respectively. It can be seen that $j_z(t)$ began with a half-cycle pulse and ended with slowly decreasing fluctuations towards zero. And $E_z(t)$ appeared in similar way, i.e., a single-cycle pulse followed by decreasing oscillations.

Impressively, the above theoretical results of EM waveforms in Fig. 1(a) and (b) are in good accordance with the experimental reports of Ref. [16], reproduced as Fig. 1(c) in this work, in both time and frequency domains. Note that, Fig. 1(c) was also obtained via the Cherenkov mechanism but in microwave band, which (by shape) resemble our theoretical results in THz band (Fig. 1(a) and (b)) due to the scaling law of the model. This could indirectly confirm the validity of our calculation method. A more proper experimental evidence should be provided in THz spectral region for sure. However, the detectable

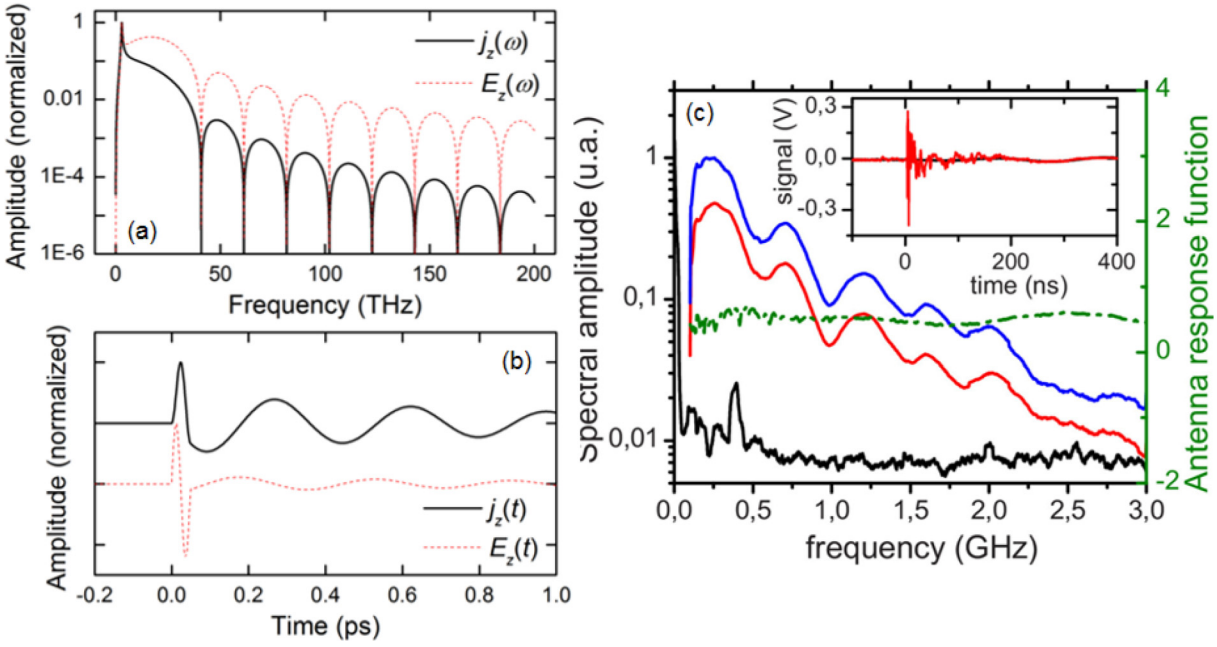

Fig. 1. The calculated longitudinal current j_z (black line) and the corresponding EM radiation E_z (red dashed line) in (a) frequency domain and (b) time domain (vertical offset for clarity) during single-colour filamentation. (c) Solid lines (from bottom to top): spectrum of the noise (black), of the measured signal (red) and of the deconvoluted signal (blue). The deconvoluted spectrum is calculated with the antenna response function presented as the dashed green line. The corresponding temporal waveforms for signal and noise are presented in the inset. (Reproduced from Ref. [16], with the permission of AIP Publishing). (For interpretation of the references to colour in this figure legend, the reader is referred to the web version of this article.)

THz bandwidth in practice is generally within tens of terahertz [26,27], much narrower than that (up to 200 THz) as shown in Fig. 1(a).

Effects of three characteristic parameters on the generated EM spectrum

In Fig. 1(a), a low-frequency sharp peak appeared in the $E_z(\omega)$ [or $j_z(\omega)$] spectrum, whose origin could be attributed to the resonance between plasma and EM waves, denoted by the first half of Eq. (2) before the multiplication sign. Furthermore, as for the step-down high-frequency components in Fig. 1(a), it is the Fourier spectrum of the laser pulse intensity [15,28], which is contributed by the second half of Eq. (2).

Thus, in this section, $E_z(\omega)$ spectrum expression [Eq. (2)] is analyzed in form of $E_z(\omega) \propto E_L(\omega) \cdot E_H(\omega)$, where $E_L(\omega)$ is the first half of Eq. (2) and simplified as

$$E_L(\omega) = i\omega\omega_{pe}^2 \frac{\omega + 2i\nu_e}{\omega_{pe}^2 - \omega^2 + i\nu_e\omega}. \tag{3}$$

One can see that $E_L(\omega)$ is mainly associated with the generated plasma during filamentation [free electron oscillation (ω_{pe}) and collision (ν_e)], accounting for the low-frequency rapid growth of the EM spectrum in Fig. 1(a). And $E_H(\omega)$ is the second half of Eq. (2), given by

$$E_H(\omega) = \frac{\sin(\omega\tau_L/2)}{1 - (\omega\tau_L/2\pi)^2} \times \exp\left(-\frac{i\omega\tau_L}{2}\right) \tag{4}$$

whose profile is solely determined by the pump laser pulse duration (τ_L), corresponding to the step-down high-frequency components of the EM spectrum in Fig. 1(a). Next, three parameters, i.e., N_e (in ω_{pe}) and ν_e of $E_L(\omega)$, and τ_L of $E_H(\omega)$, have been studied separately in the following subsections.

Free electron density (N_e)

As for $E_L(\omega)$, set N_e values increasing from 1×10^{16} to 10×10^{16} cm^{-3} within the range of the reported typical values of N_e in the literature [29]. The calculation results of $E_L(\omega)$ are shown in Fig. 2(a), from which one can see the blue shift of the location of the spectral peak. This phenomenon could be explained by the resonance between the plasma and the EM waves.

Firstly, the frequency locations of the $E_L(\omega)$ spectral peaks shown in Fig. 2(a) have been extracted and shown in Fig. 2(b) as the black open circles (f_P). On the other hand, THz resonance frequencies (f_R) with respect to $N_e = 1 \times 10^{16}$ to 10×10^{16} cm^{-3} have been calculated via $2\pi f_R = \omega_{pe} = (e^2 N_e/m_e \varepsilon_0)^{1/2}$. And the results are also shown in Fig. 2(b) as the red line. It can be clearly seen that they closely followed each other, confirming the THz-plasma resonance during Cherenkov radiation inside the single-colour filament. That is, $E_L(\omega)$ reaches maximum when THz angular frequency $2\pi f_R$ equals to the plasma frequency ω_{pe} in case of a certain N_e value. When N_e (and also the corresponding ω_{pe}) increased, THz-plasma resonance ($2\pi f_R = \omega_{pe}$) occurred at a higher THz frequency, as shown in Fig. 2(a). Similar THz-plasma resonance phenomena were also observed in case of two-colour laser pumping [30]. In Ref. [30], THz waves with higher-frequency components have been found to be spatially confined in the inner radial positions of the cross-section of the filament plasma, so as to achieve resonance with the local plasma with higher density.

It is noteworthy that, the above THz-plasma resonance counts on relatively small value of the electron collision frequency compared to the plasma frequency, i.e., $\nu_e < \omega_{pe}$ [24]. In this situation, the dominant term in the expression of $E_L(\omega)$ [Eq. (3)] is the denominator which could be around zero when ω approaches ω_{pe}, and the spectrum could reach maximum (THz-plasma resonance), consequently. Remind ourselves that, in the above calculations, ν_e was fixed at 2 THz, while ω_{pe} was above 5.64 THz with $N_e = 10^{16-17}$ cm^{-3}. Although one can hardly vary N_e without changing ν_e, it is here for a quick look at the leading role of each parameter.

One may also notice that, while increasing the N_e value, the full width at half maximum (FWHM) of the $E_L(\omega)$ peak changed little (slightly decreased from 0.7 to 0.58 THz), as indicated in Fig. 2(b) as the blue solid squares. This is very different from the case of varying ν_e, which will be introduced in the next subsection.

Electron collision frequency (ν_e)

In this section, ν_e in $E_L(\omega)$ has been varied to study its influence on the output EM spectral peak. As can be seen in Fig. 3(a), when ν_e increased from 1 to 10 THz, the location of the spectral peak remained almost the same at around 2.8 THz, while its width strongly broadened. These two tendencies have been quantified in Fig. 3(b) as black open circles and blue solid squares, respectively.

The above phenomena can be explained roughly from the point of view of mathematics, that the formula of $E_L(\omega)$ [Eq. (3)] is similar with a line-shape function of an emission spectrum [31]:

$$I(\omega) = \frac{1}{\pi} \frac{\gamma}{(\omega - \omega_0 - \beta)^2 + \gamma^2} \tag{5}$$

where ω is the angular frequency of the radiation and ω_0 is the undisturbed angular frequency. β is the angular frequency shift and γ is half the FWHM of the spectrum.

In Eq. (3), ν_e somehow plays the role of the spectral line width γ in Eq. (5). Thus when ν_e increased, the width of spectral peak (FWHM) grew simultaneously, as shown in Fig. 3(a). In the same figure, however, f_P remained nearly unchanged, since it is determined by ($\omega_0 + \beta$) in Eq. (5), or N_e (ω_{pe}) in Eq. (3), which was set to be 10^{17} cm^{-3}. Moreover, the broadening of $E_L(\omega)$ via increasing ν_e might also be regarded as a phenomenological "collision broadening" of the EM radiation spectrum during filamentation, since ν_e represents the collision frequency of the free electron inside the plasma column.

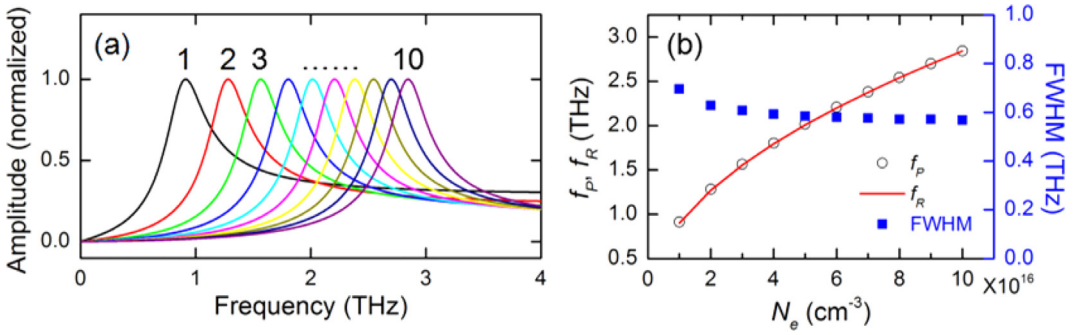

Fig. 2. (a) Normalized $E_L(\omega)$ with different N_e values ranging from 1×10^{16} to 10×10^{16} cm^{-3} (marked by 1, 2, 3 … 10). (b) The locations of the $E_L(\omega)$ spectral peak (f_P, black open circles) and the calculated THz resonance frequencies (f_R, red line) as a function of N_e. The blue solid squares represent the FWHM values of each $E_L(\omega)$ spectral peak. (For interpretation of the references to colour in this figure legend, the reader is referred to the web version of this article.)

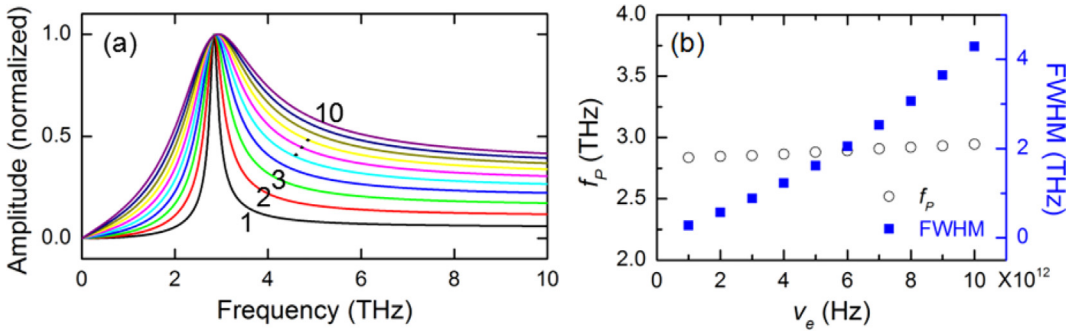

Fig. 3. (a) Normalized $E_L(\omega)$ with ν_e increasing from 1 to 10 THz (marked by 1, 2, 3 … 10). (b) The spectral locations (f_P, black open circles) and FWHM (blue solid squares) of the $E_L(\omega)$ peak as a function of ν_e. (For interpretation of the references to colour in this figure legend, the reader is referred to the web version of this article.)

Pump laser pulse duration (τ_L)

In Sections "Free electron density (N_e)" and "Electron collision frequency (ν_e)", the low-frequency peak of the $E_z(\omega)$ spectrum, i.e., $E_L(\omega)$, has been studied in view of N_e and ν_e, respectively. In this section, we turned to the step-down high-frequency components of $E_z(\omega)$, i.e., $E_H(\omega)$ of Eq. (4), which is the Fourier spectrum of the laser pulse intensity [24,28]. As for $E_H(\omega)$, τ_L was varied from 50 to 140 fs. The results are shown in Fig. 4(a) and (b), in which both of the peak frequency f_P and FWHM of the spectrum increased with the decreasing τ_L.

Similar effects of τ_L on the EM spectrum production were also observed in case of two-colour laser pumping THz wave generation experiments, such as in Ref. [32]. Thus it is a routine to make the THz radiation more intense by compressing the laser pulse width. Besides τ_L, the resonance enhancement between plasma and THz radiation plays another significant role, leading to the THz energy burst as shown in Fig. 1(a). Therefore, more research on this issue has been performed in the following section.

Generation of longitudinal THz wave along the axis of the filament

In Sections "Free electron density (N_e)" and "Electron collision frequency (ν_e)", the effects of N_e and ν_e have been solely studied on the EM spectrum outcome, theoretically. However, in the practical situation, N_e and ν_e change simultaneously, since ν_e is a function of N_e [33,34]. Thus, in this section, we have taken this issue into account and calculated the $E_L(\omega)$ generation along the propagation axis z of the single-colour filament. Then, the results were compared with our previous experimental work [18]. Here, the experimental parameters in Ref. [18] have been adopted in the following simulations.

Firstly, we have performed numerical simulations to infer the on-axis N_e distribution of the filament. It is based on the nonlinear wave equation using the slowly varying envelop approximation written in the retarded coordinate system $\tau = t\text{-}z/v_g(\omega)$ as [35]:

$$2ik_0\frac{\partial A}{\partial z} + \Delta_\perp A + 2\left(1 + \frac{i}{\omega}\frac{\partial}{\partial t}\right)\frac{k_0^2}{n_0}(\Delta n_{Kerr} + \Delta n_{plasma})A - K_2K_0 \frac{\partial^2 A}{\partial \tau^2} - iK_0\alpha A = 0 \quad (6)$$

The above equation involves a number of optical effects such as diffraction, self-focusing, group-velocity dispersion, self-steepening as well as plasma generation and energy losses due to multi-photon/tunnel ionization. Here, A is the electric field envelope function. $v_g(\omega)$, k_0, k_2 and α represent group velocity, wave number, group velocity dispersion parameter and absorption coefficiency associated with ionization in air, respectively [35]. Similar model has been successfully used in Ref. [36]. The simulated on-axis N_e distribution within the filament area from $z = 107.5$ to 110 cm is shown in Fig. 5(a) as the black line. It can been seen that the N_e profile had a steep rising edge but a slow falling edge, which is in good agreement with the experimental results in Ref. [36].

Next, ν_e was computed with respect to N_e via the following formula [33]:

$$\nu_e = \nu_c + \nu_m \quad (7)$$

where $\nu_c \approx 2.91 \times 10^{-6}$ (ln Λ) $N_e/T_e^{3/2}$ is the electron–ion Coulomb collision frequency (in s^{-1}); $T_e \sim 1$ eV at 300 K is the electron temperature [33,34]; ln $\Lambda \sim 5$ is the Coulomb logarithm [37]; $\nu_m \approx 3.91 \times 10^{-8}\ N_a T_e^{1/2}$ is the effective electron neutral momentum transfer frequency (in s^{-1}), and $N_a = 2.7 \times 10^{19}$ cm^{-3} is the density of neutral atoms [34]. The result of ν_e given by Eq. (7) is shown in Fig. 5(a) as the blue dashed line. As expected, the variation trends for ν_e and N_e are the same.

Then, $E_L(\omega)$ has been calculated as a function of N_e and ν_e, and the results are shown in Fig. 5(b), which were further normalized as displayed in Fig. 5(c). One can see in Fig. 5(b) that the THz wave yielded most at $z = \sim$108 mm, where N_e and ν_e are both the largest [Fig. 5(a)]. Moreover, the corresponding peak frequency f_p and FWHM of $E_L(\omega)$,

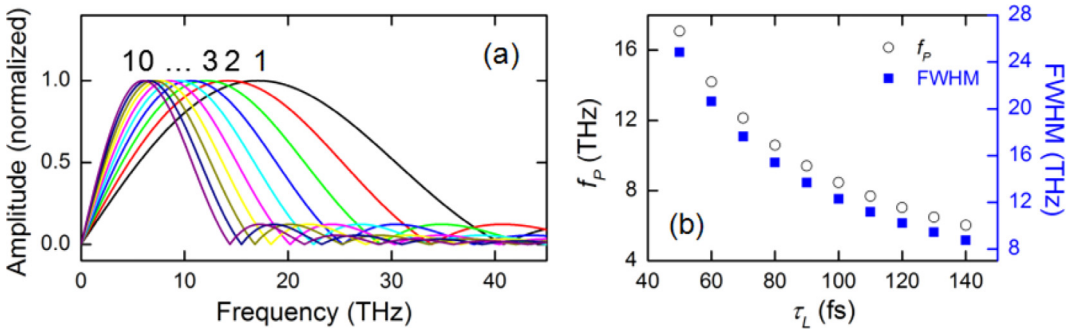

Fig. 4. (a) Normalized $E_H(\omega)$ with different τ_L values from 50 to 140 fs (marked by 1, 2, 3 … 10). (b) The locations (f_P, black open circles) and FWHM (blue solid squares) of the $E_H(\omega)$ peak as a function of τ_L. (For interpretation of the references to colour in this figure legend, the reader is referred to the web version of this article.)

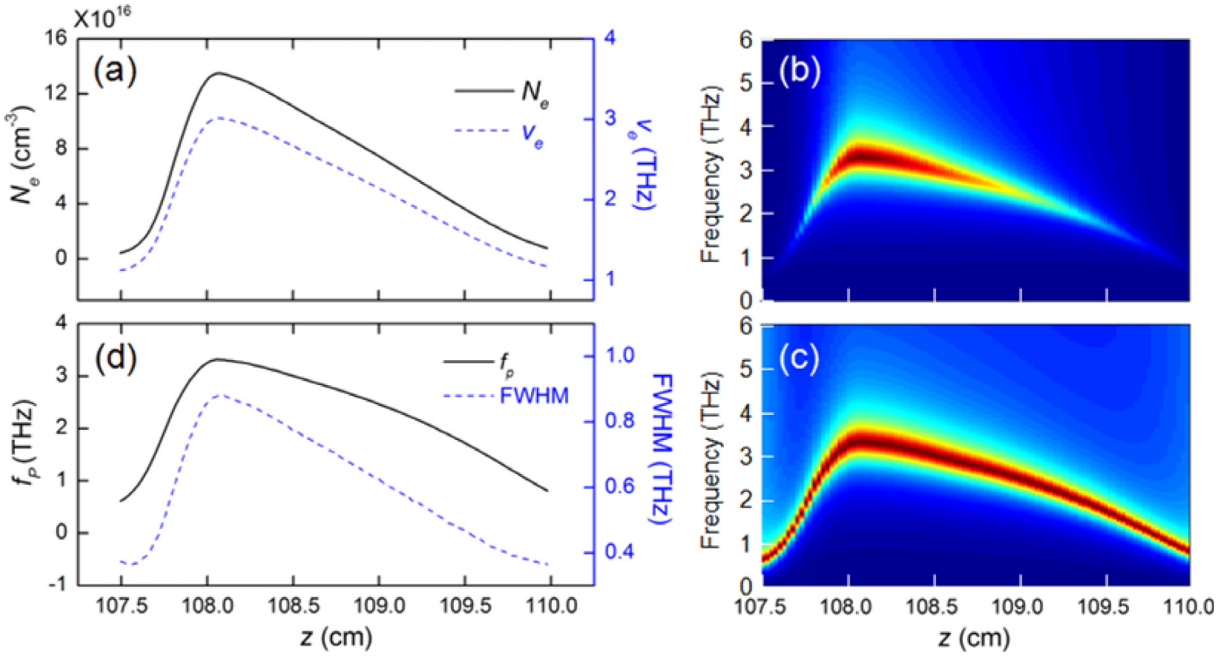

Fig. 5. (a) The simulated on-axis distributions of N_e (black line) and the corresponding v_e (blue dashed line). (b) The calculated $E_L(\omega)$ at different z along the axis of the filament. (c) The normalized results of (b) along each z point. (d) The locations (f_P, black line) and FWHM (blue dashed line) of the $E_L(\omega)$ peak as a function of z. (For interpretation of the references to colour in this figure legend, the reader is referred to the web version of this article.)

extracted from Fig. 5(c) and shown in Fig. 5(d), reached maximums at the same position ($z = \sim 108$ mm).

These features are opposite to the case of transverse THz waves detected in our previous work [17], in which both of the peak frequency and the spectral width of the transverse THz wave showed anti-correlation relationship with N_e along the filament. This phenomenon has been demonstrated to be resulted from THz wave confined propagation along the plasma channel [38]. Nevertheless, as for the longitudinal THz wave discussed in this work, it is an off-axis Cherenkov-like radiation, achieving coherence combination in the far field, which obviously cannot be constrained inside the filament like a transverse one. Therefore, it is reasonable to observe the longitudinal-transverse wave spectral differences. In addition, in time domain, more discrepancy can be noticed in the next section.

Detection of longitudinal/transverse THz pulses by EOS system

In Section "Calculation methods of EM waveforms in both time and frequency domains", EM waveforms in both time and frequency domains have been theoretically predicted, whose profile features coincided with the experimental results obtained in Ref. [16]. However, when attempting to detect this EM radiation in THz spectral range, one has to consider the limited bandwidth of a THz detector. As for the most frequently used method of recording a temporal THz signal, namely, electro-optic sampling (EOS) measurement, its available bandwidth is determined by the employed EO crystals, generally within several terahertz.

In this section, in order to calculate the detectable THz temporal waveform with an EO crystal, e.g. ZnTe, the full response function $R(\omega)$ of ZnTe has to be taken into account. According to the theoretical model developed in Refs. [39], $R(\omega)$ is given by

$$R(\omega) = \gamma_{41}(\omega) \times G(\omega) \tag{8}$$

where the EO coefficient $\gamma_{41}(\omega)$ for a ZnTe crystal is written as :

$$\gamma_{41}(\omega) = \gamma_e \times \left\{1 + C\left[1 - \frac{(h\omega)^2 - ih\omega\gamma}{(h\omega_{TO})^2}\right]^{-1}\right\} \tag{9}$$

And the response function $G(\omega)$ is written as:

$$G(\omega) = \frac{2c \times (\exp\{-i2\pi\omega d_0[n_g(\lambda_0) - n(\omega)]/c\} - 1)}{-i2\pi\omega d_0[n_g(\lambda_0) - n(\omega)][n(\omega) + 1]} \tag{10}$$

where the dielectric response of a harmonic oscillator is used to parametrize the complex refractive index $n(\omega)$ of the THz radiation:

$$n(\omega) = \sqrt{\left\{1 + \left[\frac{(h\omega_{LO})^2 - (h\omega_{TO})^2}{(h\omega_{LO})^2 - (h\omega)^2 - ih\gamma\omega}\right]\right\} \times \varepsilon_\infty} \tag{11}$$

The above parameters are adopted as: $\varepsilon_\infty = 6.7$, $\gamma = 3.01\ \mathrm{cm}^{-1}$, $C = -0.07$, $h\omega_{TO} = 177\ \mathrm{cm}^{-1}$, $h\omega_{LO} = 206\ \mathrm{cm}^{-1}$, $\gamma_e = 1$ and $n_g(\lambda_0) = 3.244$. Moreover, the experimental parameters of Ref. [18] have also been adopted as the initial parameters of the calculation, e.g. the thickness of the ZnTe crystal is set as $d_0 = 1.5$ mm.

The computing result of Eq. (8) is shown in Fig. 6(a) as the red line. It can be clearly seen that the amplitude response beyond 1 THz is little and lack of flatness, whose contribution to the final THz waveform might be neglectable. Thus, this range of the response distribution has been removed in the following calculations, as shown in Fig. 6(a) as the black dashed line.

Then, the EM radiation spectrum $E_z(\omega)$ was multiplied with the simplified amplitude response distribution of ZnTe [black dashed line in Fig. 6(a)] to obtain the detectable THz spectrum, whose amplitude distribution is shown in Fig. 6(b), together with its iFT temporal waveform (inset). Comparing the calculated THz waveform in time domain with the experimental result [18], one can see a phase difference of $\pi/2$. This can be attributed to the fact that, the experimentally recorded THz signal in Ref. [18] is a transverse THz wave, which has a universal $\pi/2$ phase difference [11,40] in contrast with the calculated longitudinal one [inset in Fig. 6(b)].

This issue has been further demonstrated by detecting both longitudinal and transverse THz pulses in the same experiment. Following Ref. [40], near-infrared femtosecond laser pulses with central wavelength of 800 nm, repetition rate of 1 kHz, pulse duration of 130 fs and energy of 7.5 mJ/pulse were used to create a single-colour filament in the air. Then, the output THz beam was collimated and refocused by a pair of off-axis parabolic mirrors. Two 1.5-μm-thick ZnTe crystals, ⟨1 0 0⟩ and ⟨1 1 0⟩ oriented, were applied at the THz focus for EO

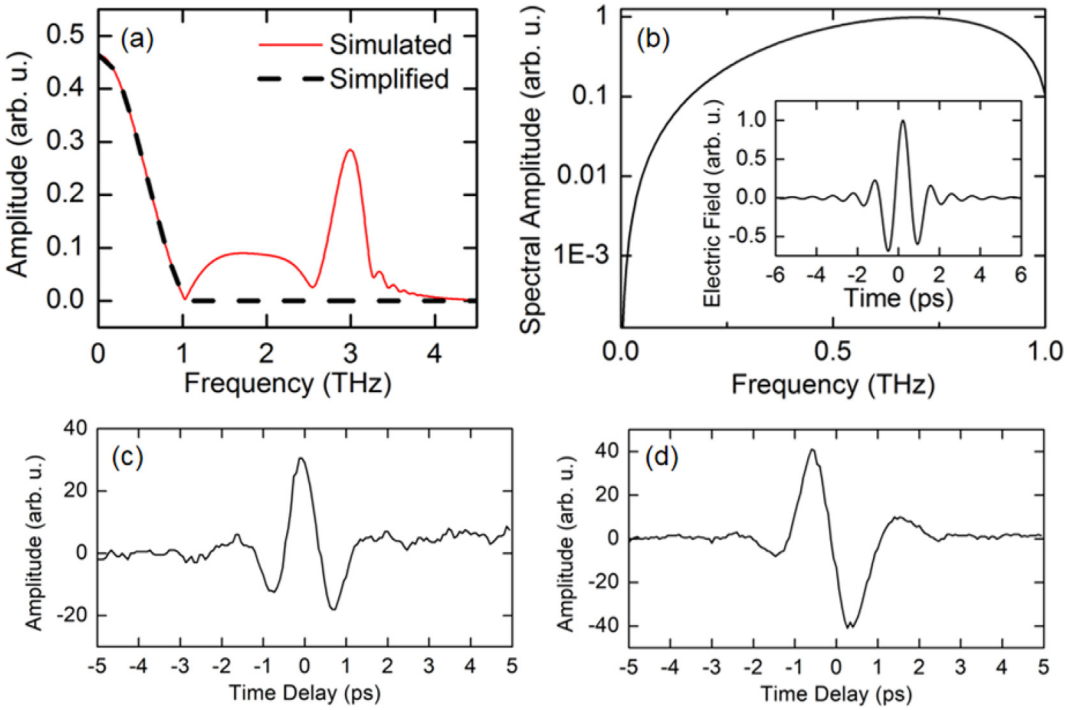

Fig. 6. (a) The simulated (red line) and simplified (black dashed line) amplitude response of a 1.5-mm-thick ZnTe crystal. (b) The calculated THz temporal pulse (inset) and spectrum sensed by the ZnTe crystal. (c) The experimental result of the longitudinal THz pulse at the focus of the emitted THz beam. (d) The transverse one in the same condition of (c). (For interpretation of the references to colour in this figure legend, the reader is referred to the web version of this article.)

sampling the longitudinal and transverse THz field components, and the results are presented in Fig. 6(c) and (d), respectively. A phase shift of π/2 can be noticed between the longitudinal and transverse THz waveforms.

The above comparison in this section has further proved the validity of our calculation method of predicting the THz waveforms in both time and frequency domains induced by longitudinal dipole oscillation during single-colour filamentation.

Enhancement of THz yield with a longitudinal external electric field

At the last part of this work, we studied the enhancement effect of a static electric field E_e, which is applied longitudinally along the filament axis, on the THz wave generation. In this case, the total electron current spectrum is a sum of two terms, i.e. $j_z^{\text{total}}(\omega) = j_z(\omega) + j_z^e(\omega)$, where $j_z(\omega)$ is the Fourier spectrum of the electron current driven by the ponderomotive force [Eq. (1)], and $j_z^e(\omega)$ is introduced by the longitudinally external electric field E_e [15]:

$$j_z^e(\omega) = \frac{\varepsilon_0 \omega_{pe}^2 E_e}{\omega^2 - \omega_{pe}^2 + i\nu_e\omega} \tag{12}$$

This time, the total EM radiation spectrum should be written as $E_z^{\text{total}}(\omega) = E_z(\omega) + E_z^e(\omega)$, where $E_z(\omega)$ is shown as Eq. (2) and $E_z^e(\omega)$ is proportional to $i\omega\, j_z^e(\omega)$:

$$E_z^e(\omega) \propto i\omega \frac{\varepsilon_0 \omega_{pe}^2 E_e}{\omega^2 - \omega_{pe}^2 + i\nu_e\omega} \tag{13}$$

Varying E_e from −2 to 2 kV/cm, the calculated amplitude of $E_z(\omega)$, $E_z^e(\omega)$ and $E_z^{\text{total}}(\omega)$ at 0.1, 0.5, 1 and 1.5 THz are shown in Fig. 7(a)–(d), respectively.

One can see that, at low THz frequency of 0.1 THz in Fig. 7(a), $E_z^{\text{total}}(\omega)$ (blue dashed line) is symmetrical with respect to E_e. This is because at 0.1 THz, $\omega \ll \omega_{pe}$, ν_e, $E_z(\omega)$ in Eq. (2) can be simplified as

$$E_z(\omega) \propto -\omega\varepsilon_0 E_L \frac{2\nu_e}{\omega_{pe}} \times \frac{\sin(\omega\tau_L/2)}{1 - (\omega\tau_L/2\pi)^2} \tag{14}$$

whose amplitude is independent on E_e [horizontal black dotted line in Fig. 7(a)] and phase is about zero [horizontal black dotted line in Fig. 7(e)]. On the other hand, $E_z^e(\omega)$ in Eq. (13) can be simplified as

$$E_z^e(\omega) \propto -i\omega\varepsilon_0 E_e \tag{15}$$

whose amplitude is symmetrical around $E_e = 0$ [red line in Fig. 7(a)] and phase varies from π/2 to -π/2 depending on the sign of E_e [red line in Fig. 7(e)]. Therefore, the phase difference between $E_z(\omega)$ and $E_z^e(\omega)$ is a constant of about 90 degree [Fig. 7(e)]. Thus, $E_z^{\text{total}}(\omega)$ [blue dashed line in Fig. 7(a)] can be symmetrical with respect to E_e. These results agreed well with the experimental reports in Ref. [15].

However, what is not involved in Ref. [15] is that, with the growth of THz frequency (0.5, 1, 1.5 THz), $E_z^{\text{total}}(\omega)$ gradually became asymmetrical, as can be seen in Fig. 7(b)–(d). This phenomenon can be interpreted by the fact that, when ω increased to a larger value above 0.1 THz, the amplitude and phase of $E_z(\omega)$ changed remarkably. Especially, the phase of $E_z(\omega)$ is no longer zero as shown as the black dotted lines in Fig. 7(f–h). On the other hand, the phase of $E_z^e(\omega)$ changed little when ω increased, which can be noticed in Fig. 7(e–h). In view of the $E_z(\omega)$-$E_z^e(\omega)$ phase difference decreasing from Fig. 7(e) to (h) in the region of $E_e > 0$, it is expected that the final $E_z^{\text{total}}(\omega)$ outcome will be larger in the same E_e range. This is exactly what can be observed in Fig. 7(b–d). This result should be taken into consideration when applying a longitudinal external electric field along a single-colour filament, aiming at an enhancement of the THz yield.

The corresponding experimental verification was carried out with similar configurations as described in Ref. [15]. In brief, a single-colour filament in length of ~1 cm was created in the air as the source of THz radiation, longitudinally along which a static electric field E_e could be varied between −2 and +2 kV. The enhanced THz emission was collected into a Golay cell detector (Tydex). Meanwhile, a band-pass filter centered at 0.1 (or 0.3, 0.5) THz (Tydex) was positioned before the detector's entrance. The experimental results are shown in Fig. 8(a–c) at

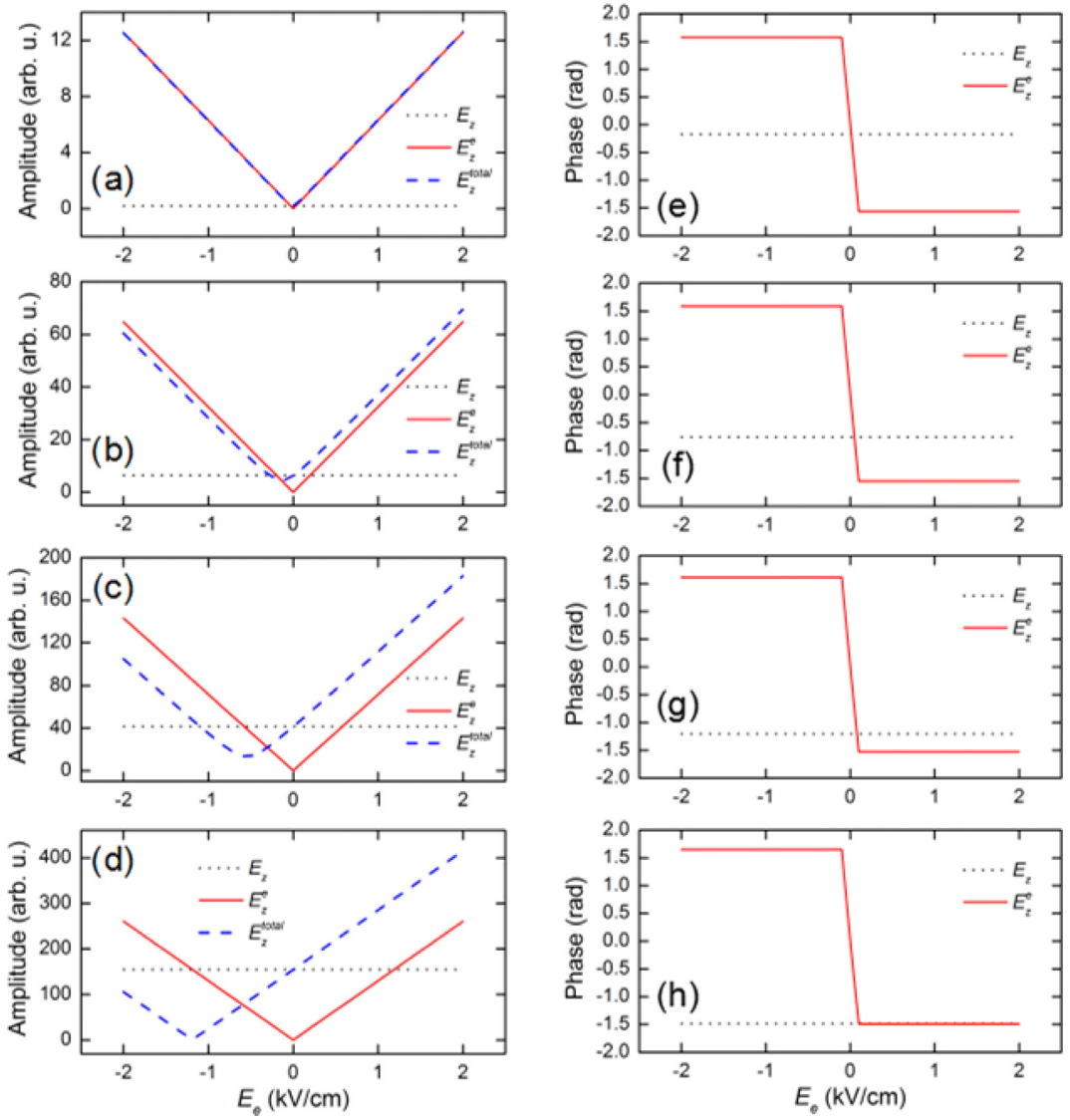

Fig. 7. The calculated amplitudes of $E_z(\omega)$, $E_z^e(\omega)$ and $E_z^{total}(\omega)$ as a function of E_e at $\omega/2\pi$ equaling (a) 0.1, (b) 0.5, (c) 1 and (d) 1.5 THz. The corresponding phase variations of $E_z(\omega)$ and $E_z^e(\omega)$ as a function of E_e at ω/π equaling (e) 0.1, (f) 0.5, (g) 1 and (h) 1.5 THz.

0.1, 0.3 and 0.5 THz, respectively. One can clearly see the symmetry breaking of E_z^{total} distribution along E_e towards the higher THz frequency (Fig. 8(c)). This tendency is in good agreement with the predictions of our theory (blue dashed lines in Fig. 7). Some quantitative discrepancies between Figs. 7 and 8 could be attributed to the non-negligible bandwidth of the used filter.

Conclusion

In summary, in this work, the EM wave emission during single-colour filamentation in air has been studied via the Cherenkov mechanism in both time and frequency domains. In brief, according to the spectrum expression of the longitudinal current [15], the simultaneous EM radiation in frequency domain could be achieved via differentiation. Then the temporal EM electric field can be calculated by means of iFT. This calculation method has been successfully employed to reproduce the detected EM waveforms in previous reports [16,18], in both microwave and THz bands. Furthermore, the generated THz spectrum along the axis of the plasma filament and the enhanced THz amplitude output with a longitudinal static electric field along the

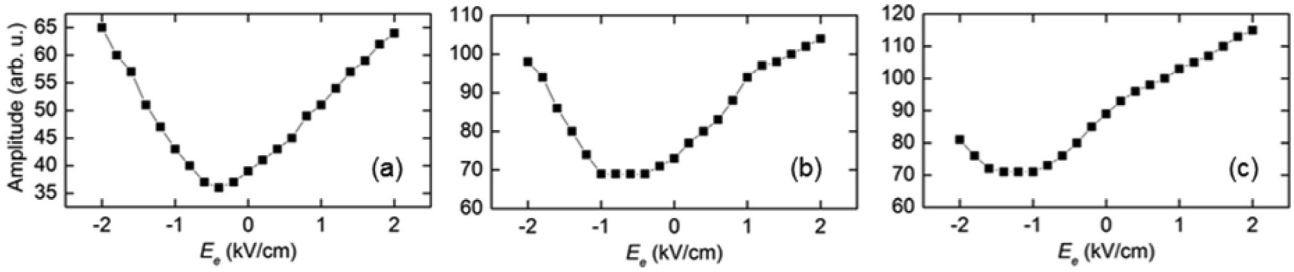

Fig. 8. The recorded amplitudes of $E_z^{total}(\omega)$ as a function of E_e after the band-pass filter centered at (a) 0.1, (b) 0.3 and (c) 0.5 THz.

filament have also been theoretical predicted, consistent with the experimental results in the literature [15,17] or of ourselves. The validity of our calculation method proved in this paper could ensure promising applications, such as computing the physical process of particle acceleration or particle control in longitudinal THz electric field when a plasma filament is adopted as the THz source.

Acknowledgments

This work was supported by National Key R&D Program (213) of China, Shanghai Chenguang Project (18CG53) and National Natural Science Foundation of China (11704252).

Disclosure statement

No potential conflict of interest was reported by the authors.

References

[1] Payeur S, Fourmaux S, Schmidt BE, MacLean JP, Tchervenkov C, Kieffer JC. Generation of a beam of fast electrons by tightly focusing a radially polarized ultrashort laser pulse. Appl Phys Lett 2012;101(4):041105https://doi.org/10.1063/1.4738998.
[2] Wang H, Shi L, Lukyanchuk B, Sheppard C, Chong CT. Creation of a needle of longitudinally polarized light in vacuum using binary optics. Nat Photonics 2008;2(8):501–5. https://doi.org/10.1038/nphoton.2008.127.
[3] Meier M, Romano V, Feurer T. Material processing with pulsed radially and azimuthally polarized laser radiation. Appl Phys 2007;86(3):329–34. https://doi.org/10.1007/s00339-006-3784-9.
[4] Skelton SE, Sergides M, Saija R, AIatì M, Maragó OM, Jones PH. Trapping volume control in optical tweezers using cylindrical vector beams. Opt Lett 2013;38(1):28–30. https://doi.org/10.1364/ol.38.000028.
[5] Biss DP, Youngworth KS, Brown TG. Dark-field imaging with cylindrical-vector beams. Appl Opt 2006;45(3):470–9. https://doi.org/10.1364/AO.45.000470.
[6] Minami Y, Kurihara T, Yamaguchi K, Nakajima M, Suemoto T. Longitudinal terahertz wave generation from an air plasma filament induced by a femtosecond laser. Appl Phys Lett 2013;102(15):151106https://doi.org/10.1063/1.4802482.
[7] Chang G, Divin CJ, Liu CH, Williamson SL, Aalvanauskas G, Norris TB. Generation of radially polarized terahertz pulses via velocity-mismatched optical rectification. Opt Lett 2007;32(4):433–5. https://doi.org/10.1364/OL.32.000433.
[8] Konishi K, Kuwata-Gonokami M, Kanda N. Terahertz vector beam generation using segmented nonlinear optical crystals with threefold rotational symmetry. Opt Express 2012;20(20):21896–904. https://doi.org/10.1364/OE.20.021896.
[9] Waselikowski S, Fischer C, Wallauer J, Walther M. Optimal plasmonic focusing on a metal disc under radially polarized terahertz illumination. New J Phys 2013;15(7):075005https://doi.org/10.1088/1367-2630/15/7/075005.
[10] Kan K, Yang J, Ogata A, Sakakihara S, Kondoh T, Norizawa K, et al. Radially polarized terahertz waves from a photoconductive antenna with microstructures. Appl Phys Lett 2013;102(22):221118https://doi.org/10.1063/1.4809756.
[11] Winnerl S, Hubrich R, Mittendorff M, Schneider H, Helm M. Universal phase relation between longitudinal and transverse fields observed in focused terahertz beams. New J Phys 2012;14(14):103049–60. https://doi.org/10.1088/1367-2630/14/10/103049.
[12] Winnerl S, Zimmermann B, Peter F, Schneider H, Helm M. Terahertz Bessel-Gauss beams of radial and azimuthal polarization from microstructured photoconductive antennas. Opt Express 2009;17(3):1571–6. https://doi.org/10.1364/OE.17.001571.
[13] D'Amico C, Houard A, Franco M, Prade B, Mysyrowicz A, Couairon A, et al. Conical forward THz emission from femtosecond-laser-beam filamentation in air. Phys Rev Lett 2007;98(23):235002https://doi.org/10.1103/PHYSREVLETT.98.235002.
[14] Wu HC, Meyer-ter-Vehn J, Ruhl H, Sheng ZM. Terahertz radiation from a laser plasma filament. Phys Rev E 2011;83(3):036407https://doi.org/10.1103/PhysRevE.83.036407.
[15] Liu Y, Houard A, Prade B, Mysyrowicz A, Diaw A, Tikhonchuk VT. Amplification of transition-Cherenkov terahertz radiation of femtosecond filament in air. Appl Phys Lett 2008;93(5):051108https://doi.org/10.1063/1.2965612.
[16] Forestier B, Houard A, Durand M, André YB, Prade B, Dauvignac JY, et al. Radiofrequency conical emission from femtosecond filaments in air. Appl Phys Lett 2010;96:141111https://doi.org/10.1063/1.3378266.
[17] Zhao JY, Gao H, Li SC, Liu C, Chen YM, Peng Y, et al. Investigating the nonradially polarized component of terahertz wave emission during single-colour femtosecond laser filamentation in air. J Opt 2018;20:105502https://doi.org/10.1088/2040-8986/aadef7.
[18] Zhao JY, Zhang YZ, Wang Z, Chu W, Zeng B, Liu WW, et al. Propagation of terahertz wave inside femtosecond laser filament in air. Laser Phys Lett 2014;11(9):095302https://doi.org/10.1088/1612-2011/11/9/095302.
[19] Cherenkov PA. C.R. Acad. Sci. U.S.S.R. 1934;2:451.
[20] Frank I, Tamm ICR. Acad Sci USSR 1937;14:109.
[21] RuzicKa J, Zrelov VP. Optical transition radiation in a transparent medium and its relation to the Vavilov-Cherenkov radiation. Czech J Phys 1993;43(5):551–67. https://doi.org/10.1007/bf01589740.
[22] Galyamin SN, Tyukhtin AV, Kanareykin A. Reversed cherenkov-transition radiation by a charge crossing a left-handed medium boundary. Phys Rev Lett 2009;103(19):194802https://doi.org/10.1103/PhysRevLett.103.194802.
[23] Lin X, Easo S, Shen Y. Controlling Cherenkov angles with resonance transition radiation. Nat Phys 2018;14:816–21. https://doi.org/10.1038/s41567-018-0138-4.
[24] D'Amico C, Houard A, Akturk S, Liu Y, Le Bloas J, Franco M, Prade BB, Couairon A, Tikhonchuk VT, Mysyrowicz A. Forward THz radiation emission by femtosecond filamentation in gases: theory and experiment. New J Phys 2008;10(1):13015. https://doi.org/10.1088/1367-2630/10/1/013015.
[25] Kim KY, Glownia JH, Taylor AJ, Rodriguez G. Terahertz emission from ultrafast ionizing air in symmetry-broken laser fields. Opt Express 2007;15(8):4577–84. https://doi.org/10.1364/OE.15.004577.
[26] Kim KY, Taylor AJ, Glownia JH. Coherent control of terahertz supercontinuum generation in ultrafast laser-gas interactions. Nature Photon 2008;2(10):605–9. https://doi.org/10.1038/nphoton.2008.153.
[27] Andreeva VA, Kosareva G, Panov NA, Shipilo DE, Solyankin PM. Ultrabroad terahertz spectrum generation from an air-based filament plasma. Phys Rev Lett 2016;116(6):063902https://doi.org/10.1103/PhysRevLett.116.063902.
[28] Coherent Mitryukovskiy S. Secondary radiation from femtosecond laser filaments. Bibliographie Réf 2014.
[29] Théberge F, Liu W, Simard PT, Becker A, Chin SL. Plasma density inside a femtosecond laser filament in air: strong dependence on external focusing. Phys Rev E 2006;39(10):1290–384. https://doi.org/10.1063/1.4896722.
[30] Zhao JY, Chu W, Wang Z, Peng Y, Gong C, Lin L, et al. Strong spatial confinement of terahertz wave inside femtosecond laser filament. ACS Photonics 2016;3:2338–43. https://doi.org/10.1021/acsphotonics.6b00512.
[31] Hindmarsh WR, Petford AD, Smith G. Interpretation of collision broadening and shift in atomic spectra. Proc R Soc Lond A 1967;297(449):296–304. https://doi.org/10.1098/rspa.1967.0068.
[32] Bartel T, Gaal P, Reimann K, Woerner M, Elsaesser T. Generation of single-cycle THz transients with high electric-field amplitudes. Opt Lett 2005;30(20):2805–7. https://doi.org/10.1364/OL.30.002805.
[33] Alshershby M, Hao Z, Lin J. Guiding microwave radiation using laser-induced filaments: the hollow conducting waveguide concept. J Phys D 2012;45(26):265401https://doi.org/10.1088/0022-3727/45/26/265401.
[34] Musin RR, Shneider MN, Zheltikov AM, Miles RB. Guiding radar signals by arrays of laser-induced filaments: finite-difference analysis. Appl Opt 2007;46(23):5593–7. https://doi.org/10.1364/AO.46.005593.
[35] Zeng B, Chu W, Gao H, Liu WW, Li GH, Zhang HS, et al. Enhancement of peak intensity in a filament core with spatiotemporally focused femtosecond laser pulses. Phys Rev A 2011;84(6):063819https://doi.org/10.1103/PhysRevA.84.063819.
[36] Chen YH, Varma S, Antonsen TM, Milchberg HM. Direct measurement of the electron density of extended femtosecond laser pulse-induced filaments. Phys Rev Lett 2010;105(21):215005https://doi.org/10.1103/PhysRevLett.105.215005.
[37] https://en.wikipedia.org/wiki/Coulomb_collision#Coulomb_logarithm.
[38] Zhao JY, Liu WW, Li SC, Lu D, Zhang YZ, Peng Y, et al. Clue to a thorough understanding of terahertz pulse generation by femtosecond laser filamentation. Photonics Res 2018;6(4):296–306. https://doi.org/10.1364/prj.6.00296.
[39] Leitenstorfer A, Hunsche S, Shah J, Nuss MC, Knox WH. Detectors and sources for ultrabroadband electro-optic samplingm: Experiment and theory. Appl Phys Lett 1999;74(11):1516. https://doi.org/10.1063/1.123601.
[40] Peng Y, Geng T, Zang XF, Chen L, Zhu YM. Completely evolution of Gouy phase shift in longitudinal terahertz wave. Infrared, Millimeter, and Terahertz waves (IRMMW-THz) 2016 41st International Conference on IEEE 1-2 https://doi.org/10.1364/ISUPTW.2016.IW3B.1.